Available online at www.sciencedirect.com

SCIENCE DIRECT®

Computers and Structures 82 (2004) 1333–1347

Computers & Structures

www.elsevier.com/locate/compstruc

Mesolevel analysis of the transition region formation and evolution during the liquid composite molding process

Zuzana Dimitrovová [a,*], Suresh G. Advani [b]

[a] Department of Mechanical Engineering, ISEL and IDMEC, Instituto Superior Técnico, Av. Rovisco pais, 1049-001 Lisbon, Portugal

[b] Department of Mechanical Engineering and Center for Composite Materials, University of Delaware, 126 Spencer Lab, Newark, DE 19716, USA

Received 10 March 2004; accepted 12 March 2004
Available online 8 June 2004

Abstract

Liquid Composite Molding is a composite manufacturing process in which fiber preforms consisting of stitched, woven or braided bundles of fibers, known as fiber tows, are stacked in a closed mold and polymeric resin is injected to impregnate all the empty spaces between the fibers. An important step is to ensure wetting and saturation of all the fiber tows and regions in between them. Mesolevel analysis refers to study at the order of a fiber tow. Numerical simulations at the mesolevel are conducted by incorporating the governing equations for free boundary flows around and inside a fiber tow into a set of subroutines. The simulation can track the advancement of the resin front promoted by both hydrodynamic pressure gradient and capillary action. Efficiency and appropriateness of several stabilization techniques is explored. Numerical results are in good agreement with reported experimental studies. The results clearly show that wicking flow plays an important role at the mesolevel and cannot be omitted.

Keywords: Liquid composite molding; Free boundary flows; Mesolevel analysis; Darcy's law; Brinkman's formulation; Tow infiltration delay and advance; Wicking flows

1. Introduction

Liquid Composite Molding (LCM) is a class of low injection pressure processes in which a pre-placed dry fiber preform is held stationary in the mold (the mold may have two rigid surfaces or one rigid and one flexible face) and a thermoset resin is injected into it to cover the empty spaces between the fibers. LCM processes such as Resin Transfer Molding (RTM) and Vacuum Assisted Resin Transfer Molding (VARTM) are widely used to manufacture advanced composites with continuous fiber reinforcements [1]. Resin infiltration into the fiber preform must be carefully controlled in order to avoid poor wetting and to minimize residual voids content, which can be detrimental to the performance of the fabricated parts. Resin can be allowed to cure only after the injection is complete. Therefore one of the main objectives of the related fluid flow analysis is the determination of the free boundary advance pattern, together with identification of regions of probable voids or dry spots occurrence.

Fiber preforms are usually composed by knitted or woven layers from fiber tows which allows one to create composites with very high fiber volume fractions and tailor their mechanical properties to meet the requirements. On the other hand, this type of fiber preform forms not single but a dual scale porous medium because the spaces between the fibers are of the order of fiber diameter which is around 5–20 μm while the spaces

* Corresponding author. Fax: +351-218417915.
E-mail address: zdimitro@dem.ist.utl.pt (Z. Dimitrovová).

0045-7949/$ - see front matter
doi:10.1016/j.compstruc.2004.03.029

between the fiber tows are of the order of millimeters. [1] This order of magnitude difference in spacing causes the resin to impregnate the spaces in between the tows at a different rate than within the tows.

The flow at the fiber tow scale can be characterized as mesoscale flow. It causes non-uniformity in the resin progression, not only across the thickness, but also in the plane of the flow. Many researchers [2–8] have closely examined the mesolevel impregnation and explored various parameters related to the fiber tow filling delay or advance. In addition, simplified analytical formulae determining these parameters were established for flows across fiber tows in [2,3] and for infiltration along tows in [7], however only radial flow into fiber tows is considered, therefore final formula in [7] assumes filling delay solely. Other analytical studies are presented in [9,10], but again only radial filling is considered. Resin front progression at the mesolevel has other phenomena, which are not well understood either experimentally or theoretically and in which the role of capillarity action may play a crucial role [11].

We define *transition region* as a region formed along the macroscopic boundary or in the neighborhood of dry spots, where the flow has not yet stabilized (more details about this definition will be given later on, see also [12]). *Partially saturated region*, on the other hand refers to a region where the empty spaces between the fiber tows or within intra-tow spaces has been occupied by the resin but has not entirely filled the empty space between the fibers. In this article, we summarize some of the reasons for the formation of the transition region and predict them by mesolevel numerical simulations of the resin advancement along and across fiber tows. Numerical results are calculated by Free Boundary Program (FBP) and show good agreement with the experimental data presented in [2–8], especially regarding the flow front shape. There are still not sufficient experimental data available, allowing one to predict the fiber tows impregnation delay or advance, as a function of the inlet pressure or flow rate and material parameters such as resin viscosity, surface tension and contact angle, inter- and intra-tow porosity, and fiber diameter. Currently, as FBP can address flow in two dimensions, flow across fiber tows is analyzed in transverse direction and along fiber tows in rotational symmetry. Isothermal conditions were chosen in order to draw conclusions independently of the viscosity variation due to changes in temperature.

Additional benefits from these simulations are that one can determine the requirements on the resin properties and process conditions for favorable filling without the danger of void formation by imposing properties and conditions that will cause the flow front to stay uniform. Also one can detect possible filling anomaly that originate at the microlevel and cannot be represented at the macrolevel filling simulation with macroscopic variables. FBP results have been published for microlevel filling along with first methodologies for relative permeability and homogenized capillary pressure determination under restriction conditions in [12]. Currently, FBP can handle micro- and mesolevel filling, its efficiency of calculation was improved by inclusion of several stabilization techniques, improving not only the speed of calculation but also the accuracy of calculations. In simulations, it will be clearly shown that wicking flow plays an important role and cannot be omitted at the mesolevel scale.

Not much work has been done so far in modeling free boundary viscous flows at the mesolevel in the LCM manufacturing processes. Many simulations available nowadays in other fields of research are applicable to inviscid fluids and popular method of smoothed particle hydrodynamics could hardly be applicable here. To our knowledge only simulations by Lattice Boltzman method [13] can handle time-dependent mesolevel filling but they require a very different approach. However, due to the numerical stability of the method, the authors did not include homogenized capillary pressure inside the fiber tows but instead used surface tension influence of the same level as in inter-tow spaces. FBP can deal with any level of capillary pressure inside the fiber tows.

2. Physics and governing equations of the macrolevel infiltration

Physically, the resin movement is promoted by pressure gradient and capillary action and resisted by viscous forces. With this in mind, it is useful to separate the pressure in the hydrodynamic part (corresponding to the externally applied contribution) and the capillary part (resulting from the surface tension effect). Resin impregnation or infiltration is modeled as a liquid flowing though a porous medium. At the macrolevel, Darcy's law, as an exact homogenization result for macrolevel analysis when incompressible Newtonian resin slowly flows at microlevel under steady state conditions [14,15] is commonly used in numerical simulation codes. As most of the fabricated parts are thin, 3D simulations are usually simplified by introduction of a through-the-thickness averaged permeability [16]. Fixed mesh algorithms are more common than moving mesh ones. In standard approaches sharp flow front is assumed and the new flow front is determined from frontal velocities under quasi steady state condition by CV/

[1] In homogenization terminology, a basic cell at the microscale (the scale of the fibers) is approximately two to three orders of magnitude smaller than a basic cell at the mesoscale (the scale of the fiber tows).

FEM (control volume finite element method [17]), CE/FEM (control elements finite element method [18]), or VOF (volume of fluid method [19]) method. In such cases the new front is in fact calculated from the kinematic free boundary condition [20,21]:

$$\frac{Df}{Dt} = \frac{\partial f}{\partial t} + \frac{\mathbf{v}^{D}}{\phi} \cdot \nabla f = 0 \quad (1)$$

with the explicit scheme implemented. In Eq. (1) implicit function $f(\mathbf{x}(t), t) = 0$ describes the moving sharp flow front, $\mathbf{x}$ is spatial variable, t is the time, ϕ stands for the porosity of the fiber preform, ∇ for spatial gradient and Darcy's velocity $\mathbf{v}^{D}$ is the phase averaged velocity related to the intrinsic phase average $\mathbf{v}^{f}$ by $\mathbf{v}^{D} = \phi\mathbf{v}^{f}$.

Liquid advance can also be achieved by introduction of a new variable, saturation s, which modifies the continuity equation into [22,23]

$$\phi\frac{\partial s}{\partial t} = -\nabla \cdot \mathbf{v}^{D}(s) \quad (2)$$

and allows one to capture partially saturated region. Explicit time integration can be used again but also implicit approaches have been developed [22].

Although Eq. (2) is adopted by several authors, Darcy's law is rarely modified to satisfy Eq. (2) exactly. Effective (instead of absolute $\mathbf{K}$) permeability tensor $\mathbf{K}^{\mathrm{ef}}$ should be used, because the flow has not yet stabilized in the transition region and surface tension influence represented by homogenized (macroscopic) capillary pressure can be important in the flow front region. In summary, two more functions, relative permeability $k(s)$ and macroscopic capillary pressure $P_{\mathrm{c}}(s)$, both being functions of saturation, must enter into the analysis [24,25] and modify Darcy's law as shown below:

$$\mathbf{v}^{D}(s) = -\frac{k(s)}{\mu}\mathbf{K} \cdot \nabla(P(s) + P_{\mathrm{c}}(s)), \quad (3)$$

where $\mathbf{v}^{D}(s)$ can be expressed as $s\phi\mathbf{v}^{f}(s)$, μ is resin viscosity, effective permeability $\mathbf{K}^{\mathrm{ef}}(s) = k(s)\mathbf{K}$ (in anisotropic case it is better to use $K_{ij}^{\mathrm{ef}} = k_{ij}(s)K_{ij}$ (no sum), $k_{ij} \in [0, 1]$, $k_{ij}(0) = 0$ and $k_{ij}(1) = 1$) and $P(s)$ is the intrinsic phase average of the local hydrodynamic pressure $P(s) = \mathrm{s}p^{f}(s)$. $P_{\mathrm{c}}(s)$ is a macroscopic analog of the microscopic p_{c}; it obeys $P_{\mathrm{c}}(1) = 0$ and unlike p_{c}, it acts in the full transition region without being dependent on the actual "front curvature". Although the negative sign of the homogenized capillary pressure $P_{\mathrm{c}}(s)$ is usually omitted, we use it with the correct sign to be consistent with the microlevel value. Its definition can be set as $P_{\mathrm{c}} = 2\gamma\langle H\rangle$, where $\langle H\rangle$ is the averaged mean curvature and γ is the resin surface tension. In order to apply the pressure gradient in Eq. (3) functional dependence of saturation on spatial variable $\mathbf{x}$ must be known. Eqs. (2) and (3) reduce to the steady state formulation in the fully saturated region, i.e. for $s = 1$.

$P_{\mathrm{c}}(s)$ and $k(s)$ must enter macroscopic analysis as known data; therefore they must be determined elsewhere, experimentally or by exploiting homogenization techniques applied to resin progression results from micro and/or mesolevel. Experimental data on $P_{\mathrm{c}}(s)$ and $k(s)$ are available in other fields of research, but unfortunately they can hardly be used in composite manufacturing because of the very different nature of the porous medium architecture. Han in [26] implemented into macrolevel simulations both, $P_{\mathrm{c}}(s)$ and $k(s)$, estimated by suggested functions from other research fields with coefficients of these functions determined experimentally. Formation of the transition region can also be captured in macrolevel simulation by keeping track of both fronts, *primary front* in inter-tow spaces and *wick front* inside the tows [27,28].

3. Formation and evolution of the transition region

We defined transition region as a region along the macroscopic boundary, where the flow is not yet stabilized. Formation and evolution of the transition region can be detected across the thickness as well as in-plane of the components. Across the thickness, it can be studied even with macrolevel variables and the difference between the transition and partially saturated region can be clearly seen in the following example. For instance, a specimen with uniformly distributed pressure at the left end, with total length 0.3 m, two layers with equal (unrealistically high for the sake of the results clarity) thickness 0.05 m and with porosity $\phi = 0.5$ is shown in Fig. 1. One can observe two regions: the *stabilized or homogenized* and the *transition* region along the sample. The transition region corresponds to the region were the flow is not yet stabilized, i.e. in this particular case, where the transversal flow still takes place in order to equilibrate the flow into the homogenized pattern. [2] Therefore the transition region should be considered *broader* than the partially saturated region; however, this would enter in slight conflict with Eqs. (2) and (3) and therefore usually the influence of the saturated part of the transition region is neglected. In this example the averaged permeability calculated by the rule of mixtures works fine in the homogenized region, but in the transition region it overestimates the effective permeability.

[2] The term homogenized region is used because in periodic porous media the stabilized flow corresponds to the fully saturated flow with periodicity conditions applied. If inlet conditions do not allow periodicity, an initial region (more details are given in Section 4.3) can also be identified along the sample.

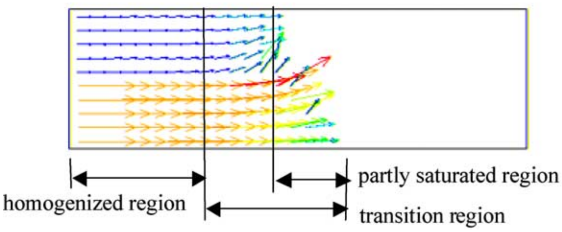

Fig. 1. Formation of the transition region across the thickness of a sample.

Origin of the transition region for the in-plane components lies in the dual porosity phenomenon and therefore the best explanation can be provided by the mesolevel analysis. The understanding can be separated into two basic flow directions: flow across and along fiber tows.

In the case of flow across the fiber tows, experimental evidence shown in [2,3,6] and numerical results presented in [13,29] clearly demonstrate that filling of the fiber tows is delayed. Resin advance, although helped by strong intra-tow capillary pressure, must overcome a fiber arrangement with much lower intra-tow permeability; thus there could hardly exist some scenario, which would move the front more or less uniformly. It is also known [30] that very high surrounding pressure acting on the tows can significantly change the single fibrils positions and actually close some spaces between them. Usually only a thin strip along the fiber tow circumference is filled when the primary resin front envelopes it, then the air is compressed inside the tow until it is balanced with the surrounding resin pressure. Hence the capillary action becomes the only factor that can drive the resin inside the tow. When the air pressure becomes higher than the surrounding pressure, the air can escape from the tow in the form of microvoids. Nevertheless this is just an academic case. If the resin is not forced to flow only across the fiber tows, it will naturally choose the easier (higher permeability) direction, i.e. along the fiber tows in this case.

In flow along fiber tows, permeability is much higher (4–90 times) and capillary action is generally twice as strong as in flow across the tows. Therefore two situations can be found in flow along fiber tows [4,5,8]. Wicking flow front inside the fiber tow can be either advanced or delayed with respect to the primary front in the inter-tow spaces, which also pre-determinates the location and shape of emerging voids (Fig. 2). Because capillary action does not depend on the externally applied inlet conditions, but it is purely a function of the resin surface tension, contact angle and geometry, these two scenarios can be explained as follows. When the externally applied pressure or flow rate is relatively high, viscous action is dominant, wicking gradient is not so strong when compared to the hydrodynamic pressure gradient and therefore inter-tow spaces (the higher permeability regions) are filled first. On the other hand, under lower externally applied action, wicking flow can become dominant and resin advances more rapidly inside the tows. There must naturally exist a situation, when these actions are "equilibrated" and resin progresses more or less uniformly. It should be remarked in this context, that higher external conditions are used with the objective to reduce the filling time, as a main cost factor. On the other hand it is well known that lower external conditions are favorable for better accomplishment of the infiltration phase and quality of the part, because sufficient time must be given to the resin–fiber interaction to form an interface increasing the adhesion between the two phases. However, in very slow filling it is conceivable that the resin will cure and solidify before all the empty pores are filled.

Transition region can be studied at the macrolevel by many techniques, and if the relative permeability

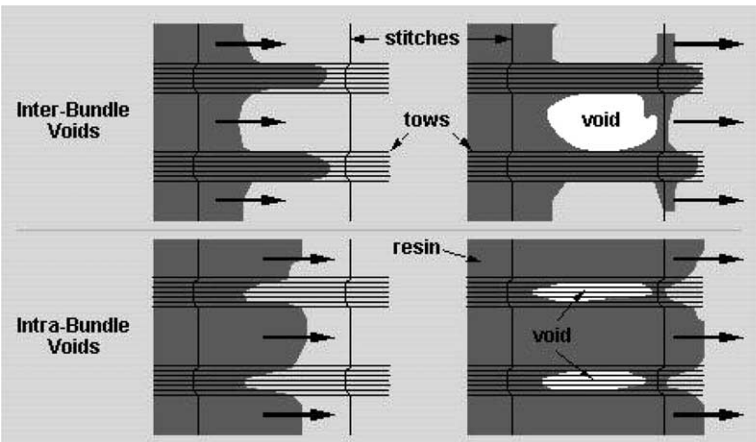

Fig. 2. Inter- and intra-tow void formation.

and homogenized capillary pressure are known, one could also use commercial software such as ANSYS (analogy with thermal analysis [31]) and ABAQUS (SOILS procedure [11,22]). These types of studies allow one to identify situations in which the intermediate region is significant and cases where the standard approaches would be sufficient. Final results allow one to study the depth of the transition region and saturation distribution, with respect to the given functions $k(s)$ and $P_c(s)$, and with dependencies on other process parameters.

In ANSYS simulation, there is no concept of relative permeability input, i.e. $k(s) \equiv 1$. In [31], pressure values are shifted by the total range of the capillary pressure. Terms initial $P_i = 0$ and saturated pressure $P_s \approx -P_c(0)$ are used and it is assumed that $c_0 \cdot P_s = \phi$ and

$$\phi \frac{\partial s}{\partial t} = c_0 \frac{\partial P}{\partial t} \approx c_0 \frac{\partial P_c}{\partial t} \tag{4}$$

are fulfilled in the transition region, where c is analogous to a fictitious "specific heat". High c_0 (and consequently low P_s) corresponds to low depth of the transition region. Both curves, P_c and s as function of spatial variable, are convex, rather than concave as in [4], Figs. 3 and 4. However, here as well as in [4] $s(x)$ is proportional to $P_c(x)$, implying that $P_c(s)$ is linear. Eq. (4) then corresponds approximately to the linear decrease in Darcy's velocity with respect to the spatial variable (Fig. 4) and the expected transition region depth, d, can be estimated from known parameters (for more details see [31]).

From ABAQUS simulations, let us present simple one-dimensional example of a porous medium 30 mm long being filled by constant in-flow velocity 0.2 mm/s. Parameters of the porous medium are: $\phi = 0.5$, $s_i = 0.012$ which will result in a theoretical filling time of 74.1 s, $K = 5.37 \times 10^{-3}$ mm^2 corresponding to the cross-section of in-line packed cylindrical fibers of diameter 1.35 mm with distances between their centers equal to 1.7 mm. The resin viscosity is $\mu = 226$ mPa s and consequently the maximum pressure, when the specimen is

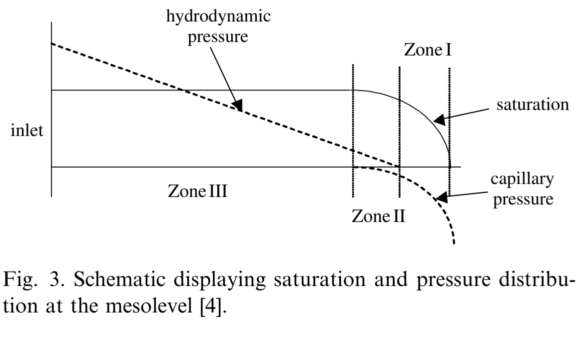

Fig. 3. Schematic displaying saturation and pressure distribution at the mesolevel [4].

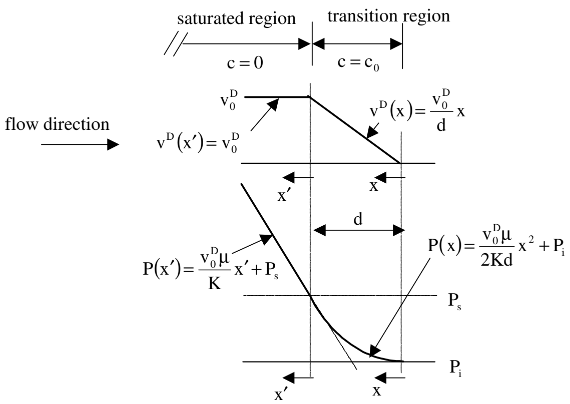

Fig. 4. Schematic illustration of the simplifying assumptions about Darcy's velocity and pressure distribution in the transition region of one-dimensional problem [31].

completely filled, is 250 Pa. Three different capillary pressure variations were chosen according to Fig. 5a (case B is plotted and cases A and C are schematically explained) and three relative permeability distributions (cases 1–3) according to Fig. 5b were selected. Case A was thus chosen as the case, where the maximum hydrodynamic and the maximum capillary pressure at initial saturation are the same. Combining all the possibilities from Fig. 6, nine different situations can be obtained, however, cases C1 and C2 did not converge and from B cases only B1 and B3 are presented, as B cases exhibit very similar results.

According to the depth of the intermediate region, the cases can be arranged in descending order as follows: A3, A2, A1, B3, B1 and C3, illustrating the influence of the magnitude of the capillary pressure. Stronger the capillarity, larger is the intermediate region. Cases in C exhibit very short intermediate region, hence the convergence difficulties, and therefore one can ignore the capillary action for such cases anyway. Relative permeability influence is significant for high capillary effect (cases A), while it is almost negligible for low capillarity (cases B and C). These conclusions can be seen in Fig. 6, in which for $t = 40$ s the pressure and saturation distribution along the specimen are shown for the six cases. Obviously, pressure gradient in the fully saturated part is the same for all cases (it is proportional to the inlet velocity) and integral of saturation distribution is also the same for all cases (it is proportional to the total resin volume injected until that time). It is seen again that $s(x)$ and $P_c(x)$ are rather convex than concave, and that they are not proportional, because $P_c(s)$ was not a linear function of s. For more details see [11]. It could be remarked at this point that we did not find any discrepancy between the analytical and numerical filling time as noticed in [22].

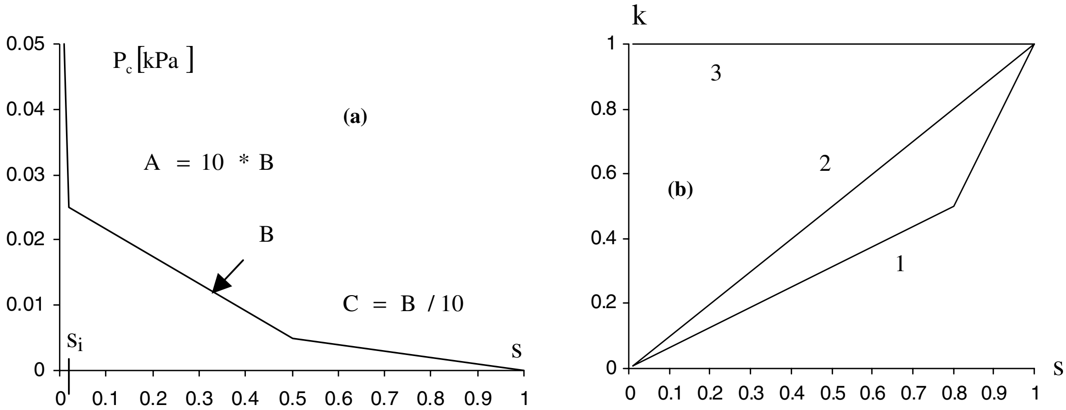

Fig. 5. (a) Homogenized capillary pressure and (b) relative permeability variation with respect to the saturation.

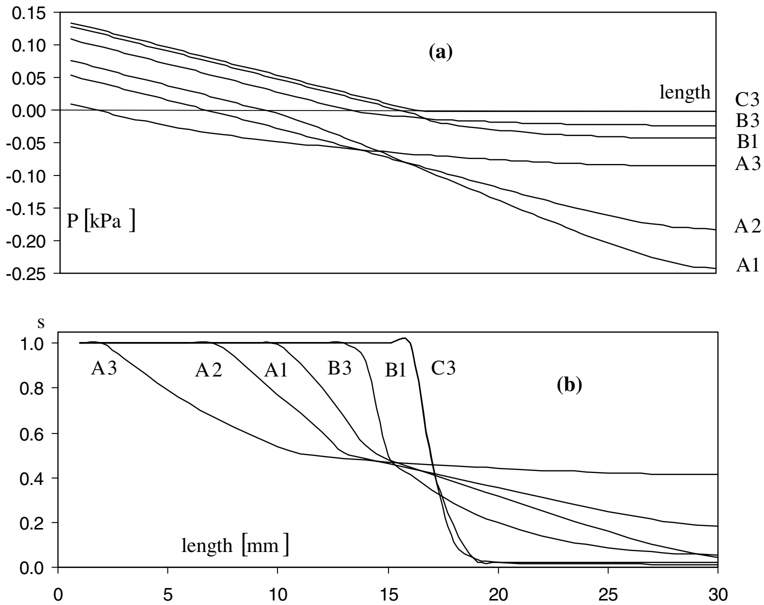

Fig. 6. (a) Pressure and (b) saturation distribution along the flow direction at $t = 40$ s.

4. Mesolevel analysis

4.1. Physics and governing equations for the mesolevel infiltration

Because of the infiltration complexity, resin flow must be studied in its time-dependent nature at all three scales: micro, meso and macro. Especially mesoscale is interesting, because it gives the best view on the transition region formation and evolution. Systematic investigation of mesoscale flow is still required in order to understand void formation mechanism and voids dynamics.

In mesolevel analysis, liquid flowing along two different scales must be considered. Single scale porous media (fiber tows) and open spaces (inter-tow spaces) are presented and therefore different flow regimes are linked together. Because fiber tows have uniformly distributed pores, sharp flow front can be assumed in the intra-tow spaces. Moreover quasi steady state assumption still holds and can be exploited. As the flow is slow, inertia terms can be neglected, implying that Stoke's problem in inter-tow spaces $\Omega^{S}_{t_k}$ and Darcy's problem in intra-tow region $\Omega^{B}_{t_k}$ have to be solved at each discretized time t_k. In fact, Darcy's law must be modified to Brinkman's equations, in order to account for viscous

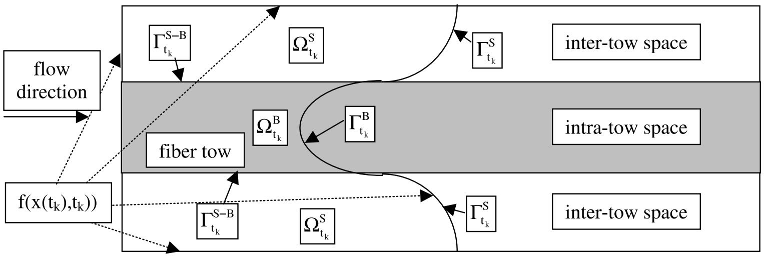

Fig. 7. Schematic of flow domain with designations related to Eqs. (5) and (6).

stress at the interface between these two regions ($\Gamma_{t_k}^{\mathrm{S-B}}$), which rapidly decreases with the distance from $\Gamma_{t_k}^{\mathrm{S-B}}$ (Fig. 7). In summary, it must be satisfied at each time step, t_k:

in inter-tow spaces:

$$\begin{aligned}&\nabla \cdot \mathbf{v} = 0\\ &\nabla p = \mu \Delta \mathbf{v} \text{ in } \Omega_{t_k}^{\mathrm{S}}\end{aligned} \quad \text{(Stoke's equations)}, \tag{5a}$$

in intra-tow spaces:

$$\begin{aligned}&\nabla \cdot \mathbf{v}^{\mathrm{D}} = 0\\ &\nabla p^f = \mu \Delta \mathbf{v}^{\mathrm{D}} - \mu \mathbf{K}^{-1} \cdot \mathbf{v}^{\mathrm{D}} \text{ in } \Omega_{t_k}^{\mathrm{B}}\end{aligned} \quad \text{(Brinkman's equations)}. \tag{5b}$$

Here $\mathbf{v}$ and p are local velocity vector and pressure, respectively, and $\Delta = \nabla \cdot \nabla$.

If fibers inside the tows are rigid, impermeable and stationary, the following boundary conditions, under usual omission of the air pressure, must be fulfilled at the free front:

$$\sigma_t^{\mathrm{v}} = 0 \text{ and } (\sigma^{\mathrm{v}} \cdot \mathbf{n}) \cdot \mathbf{n} - p = \sigma_n^{\mathrm{v}} - p \approx -p = -p_{\mathrm{c}} = -2\gamma H \quad \text{at } \Gamma_{t_k}^{\mathrm{S}}, \tag{6a}$$

$$p^f = P_{\mathrm{c}} \quad \text{at } \Gamma_{t_k}^{\mathrm{B}}, \tag{6b}$$

and progression of the free boundary can be determined according to

$$\frac{\mathrm{D}f}{\mathrm{D}t} = \frac{\partial f}{\partial t} + \mathbf{v} \cdot \nabla f = 0 \quad \text{at } \Gamma_{t_k}^{\mathrm{S}}, \tag{6c}$$

$$\frac{\mathrm{D}f}{\mathrm{D}t} = \frac{\partial f}{\partial t} + \frac{\mathbf{v}^{\mathrm{D}}}{\phi_t} \cdot \nabla f = 0 \quad \text{at } \Gamma_{t_k}^{\mathrm{B}}, \tag{6d}$$

where $\boldsymbol{\sigma}^{\mathrm{v}}$ is local viscous stress, $\mathbf{n}$ stands for the outer unit normal vector to the free front in Stoke's region $\Gamma_{t_k}^{\mathrm{S}}$, $\Gamma_{t_k}^{\mathrm{B}}$ is the free front in Brinkman's region and ϕ_t is intra-tow porosity. Other boundary conditions as symmetry, periodicity and inlet conditions are related to the particular problem under consideration.

FBP is concerned with the moving flow front, which requires results at time t_k, approximation of the front at t_k locally smoothed in order to determine outer normals for use in the kinematic free boundary condition (6c) and (6d); determination of the new resin front position at t_{k+1}, approximation of this front locally in Stoke's region by a smooth curve in order to determine its curvature; and application of boundary conditions. Then the base analysis is solved by ANSYS FLOTRAN module and the process is repeated. FBP has to deal with the usual problems of moving mesh algorithms with remeshing of the filled domain at each time step, like boundary identification, preventing of normal crossing, free boundary looping, etc.

ANSYS FLOTRAN can account for porous media influence by introduction of distributed resistance. Averaged values in Eqs. (5b), (6b), (6d) are therefore important mainly from theoretical viewpoint, while numerically either velocity or pressure maintain their meaning as nodal variable in both regions, preserving all necessary continuity requirements at $\Gamma_{t_k}^{\mathrm{S-B}}$.

Verification of the correctness of the distributed resistance introduction can be conducted in several ways. For instance, flow across in-line arrangement of cylindrical fiber tows with circular cross-section of relative radius 0.3 and intra-tow porosity $\phi_t = 0.9$ can be considered. Let each tow contains 89 fibers of relative diameter 0.02 with in-line arrangement, yielding intra-tow permeability of 1.28×10^{-4} unit^2. According to homogenization techniques permeability equals to averaged velocity when a unit macroscopic pressure gradient is imposed on a saturated basic cell containing a unit viscosity liquid. Periodicity of liquid velocity and oscillating part of the local pressure are applied at the outer boundaries, simplified by symmetry considerations. Results of velocity and pressure distribution are in agreement with expected and published results [32,33]. Dimensionless homogenized permeability is determined as 0.0131, which corresponds to the 19% increase against 0.011 of permeability of the same geometry with "impermeable tow". It should be remarked in this context, that homogenized permeability cannot depend only on ϕ_t, because dimensional factor is always important. Numerical simulation results are dependent on the "dimensional" intra-tow permeability. The same value of 1.28×10^{-4} unit^2 could be achieved e.g. for $\phi_t = 0.6$ and 10 fibers of relative diameter 0.12.

In order to support correctness of the results, local mass conservation (LMC) error is also calculated. LMC error is FBP additional calculation. The absolute value for the total fluid flux entering and exiting each FE, should be zero. The relative LMC error switches the absolute value into dimensionless number by dividing it by the square root of the FE area and by the maximum velocity component related to this element. It was verified that both absolute and relative LMC error are concentrated at the inlet/outlet boundaries, only in relative values there is slight increase along the tow outer surface, but not significant. Therefore introduction of distributed resistance is a viable way of modeling.

When free boundary progression is treated in mesolevel simulation, one has to be careful with the capillary pressure application, Eqs. (6a) and (6b), and with the interpretation of the free boundary condition, Eqs. (6c) and (6d), implying that velocities extracted in intra-tow spaces for the new front determination must be corrected by a factor $1/\phi_t$. The numerical simulation issues are clearly related to the *transition* node at the intersection $\Gamma^{S}_{t_k} \cap \Gamma^{B}_{t_k} \cap \Gamma^{S\text{–}B}_{t_k}$, where application of Eqs. (6a–b) and (6c–d) is ambiguous. In order to eliminate this ambiguity, FE mesh around the transition node is refined, conditions from Eqs. (6a) and (6b) are imposed only at proximal frontal nodes; and automatic correction of the free front to straight line using two neighboring new nodal positions, as it is shown in Fig. 8, is implemented instead of the kinematic boundary condition at the transition node.

For classification of mesolevel flows, dimensionless measures of the importance of the viscous versus capillary forces are useful. Inter-tow capillary number $N_{\rm ci}$, modified capillary number $N_{\rm cm}$ and intra-tow capillary number $N_{\rm ct}$ can be introduced. Because these numbers depend on some characteristic velocity of the problem, they can have directional character as

$$N_{{\rm ci},x} = \frac{v_x \mu}{\gamma}, \quad N_{{\rm cm},x} = \frac{v_x \mu}{\gamma \cos\theta}, \quad N_{{\rm ct},x} = \frac{v_x^{\rm D} \mu}{\gamma} = \frac{K_{xx}}{\gamma}\left|\frac{\partial P}{\partial x}\right|, \tag{7}$$

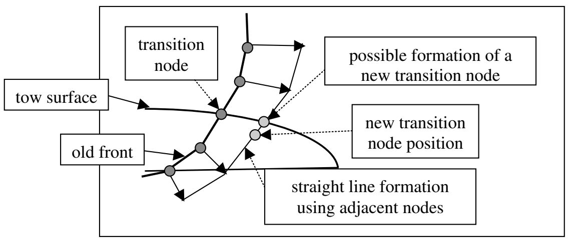

Fig. 8. Treatment of the free boundary advance at the transition node.

where v_x or $v_x^{\rm D}$ is some typical velocity of the related problem and x is permeability principal direction.

When $N_{\rm ci}$ is very low in Stoke's region, it is difficult to preserve an acceptable numerical solution. Resin front approaches constant curvature surface and although low $N_{\rm ci}$ creates more favorable conditions for injection in view of air entrapment, negative effect of low $N_{\rm ci}$ in view of numerical simulation is, that the resin front is more sensitive to the time step magnitude and unphysical non-smoothness are more probable to occur. Resin front can start to oscillate because of these factors. For better control, a maximum normal advance $\max_i \Delta x^i_{n,t_{k+1}}$ (user input) is used to calculate the actual time increase Δt_k.

Better LMC can obviously be obtained for finer FE mesh, although, application of this general knowledge is not so straightforward here. Reducing the element size and the time step Δt_k proportionally does not improve the stability of the flow front. Therefore different control must be used for different purposes. In ANSYS terminology key points are distributed evenly along the flow front and are used for the new front localization and curvature determination. They cannot be very close to each other, as this would increase the danger of unphysical non-smoothness. In this way generated frontal lines can contain several FE nodes, more nodes are used along key points touching some boundary. In addition, the maximum normal advance is reduced independently on the element size or key point distances.

Four stabilization techniques of the flow front in both regions some of which also address capillary pressure in Stoke's region are implemented in FBP in order to decrease the danger of front oscillations, increase exactness of the results and permit usage of larger maximum normal advance, which in consequence can reduce CPU time. The first stabilization technique I, is based on parameter α, relating the normal advance $\Delta x^i_{n,t_k}$ at a frontal i-point with the normal velocity v^i_{n,t_k}, as $\Delta x^{i,\alpha}_{n,t_k} = \Delta t_k \cdot v^i_{n,t_{k+\alpha}}$. In fully explicit approach $\alpha = 0$, however, more correctly it might be assumed that:

$$v^i_{n,t_{k+\alpha}} = (v^i_{n,t_k} + v^i_{n,t_{k+1}})/2 = (v^i_{n,t_k} + \beta^i_{t_k} v^i_{n,t_k})/2 = v^i_{n,t_k}(1+\beta^i_{t_k})/2, \tag{8}$$

where parameter $\beta^i_{t_k}$ can be calculated from LMC in the form:

$$R^i_{t_k} v^i_{n,t_k} = (R^i_{t_k} + \Delta x^i_{n,t_k}) v^i_{n,t_{k+1}} = \beta^i_{t_k}(R^i_{t_k} + \Delta x^i_{n,t_k}) v^i_{n,t_k}, \tag{9}$$

where $R^i_{t_k}$ is curvature radius of the free front at i-location. This procedure maintains better LMC especially in curved regions, as it can be seen in Fig. 9. An iterative algorithm according to Eqs. (8) and (9) is included in FBP, where in the first iteration radius $R^i_{t_k}$ from smooth curve approximation is implemented, while in consequent iterations areas formed by straight lines are used to update $\beta^i_{t_k}$. Number of consequent iterations can be

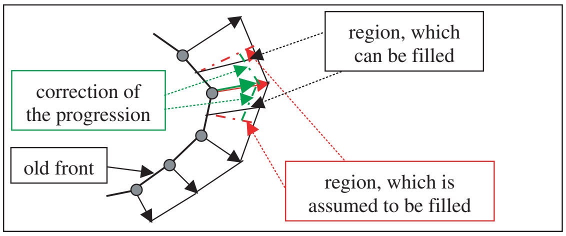

Fig. 9. Stabilization technique I of LMC for significantly curved fronts.

equal to zero in the case of fully explicit approach, when $\beta^i_{t_k} = 1\ \forall i, k$.

Stabilization technique II removes unphysical non-smoothness and it is explained in Fig. 10. When a "sharp" angle on the flow front (concept of this sharpness is determined by user specified value) is detected, the new position $\mathbf{x}^i_{t_{k+1}}$ is moved to the location in the middle of the normal line to the original (k)-front connecting intersection with a straight line between two neighboring new points $\mathbf{x}^{i-1}_{t_{k+1}}$ and $\mathbf{x}^{i+1}_{t_{k+1}}$ and the sharp location. Also this algorithm is introduced in an iterative way. It is very efficient in smoothing the front, however, no additional mass verification is included, because it is not intended as a principal techniques allowing very large normal advances.

Stabilization technique III concerns with the capillary pressure imposed on $\Gamma^S_{t_k}$. It is based on least square approximation (calculated in software Maple module) and it actually requires a rough idea about curvature variation along the front. For instance if constant curvature surface is expected, least square approximation by constant function can be used and will speed up significantly the calculation. However, if sufficient care is not taken, results can be physically unrealistic. Finally, Stabilization technique IV, smoothes the local capillary pressure values in the same way as Stabilization technique II smoothes the front. It is thus capable of preserving physical variation of the capillary pressure along the front, and therefore it is convenient in cases when curvature variation along the front cannot be guessed in advance.

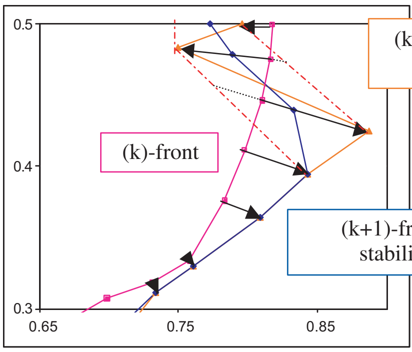

Fig. 10. Stabilization technique II eliminating unphysical non-smoothness.

4.2. Homogenized capillary pressure estimates

Fiber tows in mesolevel analysis belong to a single porous medium with uniform pore sizes, therefore transition region can be omitted and homogenized value P_c can be estimated from microlevel considerations and applied as a constant value within intra-tow spaces on $\Gamma^B_{t_k}$. If contact angle (equilibrium advancing contact angle for steady state assumption) is known, then the total capillary force can be calculated exactly by integration of "surface tension projection" along each wetted perimeter. Intrinsic phase average value P_c can be then obtained by relating the total force to the averaged pore space area. This can be done easily for flow along aligned fibers, but in flow across the fibers, fiber surface is curved and therefore except for the contact angle, an angle of the surface must be included in the projection. From literature either relation proposed by Carman, or notion of the hydraulic radius or direct implementation of Young–Laplace equation leads to [34–36]

$$P_c = S\gamma\cos\theta, \quad P_c = \frac{\gamma\cos\theta}{m}, \quad P_c = \frac{4\gamma\cos\theta}{D_e}, \tag{10}$$

where S is the ratio of the surface area of the medium to its pore volume, the hydraulic (mean) radius m is defined as the ratio of the average pore cross-sectional area to the average wet perimeter, D_e stands for equivalent diameter of the pores and θ for the contact angle. All the geometrical parameters from Eq. (8) can be estimated for particulars of the porous media. For example, in the case of flow along and across fibers, D_e is suggested in [36] in the way that:

$$P_{c,L} = \frac{4\gamma\cos\theta(1-\phi)}{\phi d_f} = 4\widetilde{P} \quad \text{and}$$
$$P_{c,T} = \frac{2\gamma\cos\theta(1-\phi)}{\phi d_f} = 2\widetilde{P}, \tag{11}$$

respectively, where d_f is the single fiber diameter. First expression in Eq. (9) does not need any estimate and can be obtained immediately from first two relations in Eq. (8). For flows across fibers, the first relation in Eq. (8) yields again $P_{c,T}(=P_{c,L}) = 4\widetilde{P}$, while, the second relation in Eq. (8) gives coefficients π or $8/\pi$ in front of $\widetilde{P}$, depending on if the average integral is calculated with respect to an angle or a distance. In our understanding (see also [12]), when resin passes a single fiber, total capillary force in the direction of the flow can be exactly calculated, once the contact point is known. Then after expressing the pore space, the intrinsic average $P_{c,T}$, either integrated over an angle or a distance, yield the same value as in [36] $P_{c,T} = 2\widetilde{P}$; hence Eq. (9) will be implemented in our examples.

4.3. FBP mesolevel results for flow along fiber tows

Fiber tows with circular cross-sections could only be studied, because of the rotational symmetry. Three different inlet situations were chosen and applied on a specimen 4 mm long with external radius of 0.5 mm and tow radius of 0.35 mm. Case A was constant inlet pressure 2 kPa. Case B was constant inflow velocity of 10 mm/s forced to have the same phase averaged value in intra-tow spaces as well and Case C was constant inflow velocity 10 mm/s allowed to decrease in the intra-tow spaces by the porosity value. Each of these cases were studied for high (case I: 1.6×10^{-3} mm^2) and low (case II: 1.6×10^{-5} mm^2) permeability values, while the porosity, viscosity, surface tension and contact angle were kept the same for all situations as 0.4, 50 mPa s, 25 mN/m and 0°, respectively. This means that in cases I single fibers have diameter of 0.08 mm and intra-tow capillary pressure corresponds to 1.9 kPa, while in cases II these values are 0.62 mm and 0.24 kPa, respectively. Higher permeability is therefore obtained by bigger fibers, which consequently decreases homogenized capillary pressure.

Flow front pattern, pressure for intermediate stages and wicking front delay or advance Δz (calculated as top advance in Stoke's region minus advance on the rotational symmetry axis, i.e. positive for filling delay) are shown in Figs. 11–13, for cases AI, AII, BI, BII, CI, CII, respectively.

Case AI shows typical tow filling delay with front shape which compares well with experimental results from [8]. When comparing wick front delay in cases AI ($\sim$1 mm) and AII ($\sim$0.1 mm), there is an order of magnitude difference as predicted by formula presented in [6–8]:

$$\Delta z = d_{\mathrm{t}}\sqrt{\frac{K_{\mathrm{i}}^{\mathrm{ef}}}{K_{\mathrm{t,r}}}}, \tag{12}$$

where d_{t}, $K_{\mathrm{i}}^{\mathrm{ef}}$ and $K_{\mathrm{t,r}}$ stand for tow diameter, effective inter-tow and radial intra-tow permeability, respectively, under assumption that $K_{\mathrm{i}}^{\mathrm{ef}}$ is the same for AI and AII. Eq. (12) with rough estimate of effective inter-tow permeability predicts wick front delay as 8 and 0.8 mm for cases AI and AII, respectively. The discrepancy from numerical prediction is related to the fact, that Eq. (12) does not consider longitudinal wicking flows, which are present in our examples and which can significantly reduce the infiltration delay. Eq. (12) shows good agreement with experimental data and was also tested for cases with high hydrodynamic pressure gradient, where longitudinal wicking flows are insignificant.

When wicking front is only slightly advanced (cases AII, BI and CI), an additional advance close to the tow surface inside the tow can be seen (Fig. 11). This might be caused by the fact, that we used isotropic permeability and did not decrease the radial value with respect to the longitudinal one. In real situations, moreover, some spaces between fibers near the tow surface could be closed because of the acting pressure, and resin could thus spread over the tow surface. This case cannot be captured by simulation with "ideal" parameters. We did not pay much attention to these situations, because in unidirectional fabrics it is also natural, that initial pore spaces close to the tow surface might be larger.

When intra- and inter-tow fronts completely separate (cases BII and CII), which can happen only in tow filling advance, flow out of the tows are neglected in numerical simulations, because it can be assumed that in such case capillary action is so strong that it would keep the resin inside the tow. On the other hand, presence of these flows would give larger possibility to voids formation. In our simulations wick front is practically straight in BII case, while in CII case (which has more natural inlet conditions) it exhibits slight curvature, as reported experimentally [4,5].

All cases B and C have the same $N_{\mathrm{cm}} = N_{\mathrm{ci}} = 0.02$. Therefore their classification should be done in terms of N_{ct}. It turned out to be quite difficult to estimate N_{ct} in a way to link similar front patterns together.

It can be concluded that tow infiltration cannot be ensured only by radial flows. Cases with equilibrated flow front or advanced wick front, which are confirmed experimentally in [4,5], and which are shown here in numerical simulations, cannot be justified without longitudinal wicking flows inside intra-tow spaces. These longitudinal flows are not pressure driven as can be concluded from pressure distribution shown in Fig. 12.

4.4. FBP mesolevel results for flow across fiber tows

In experiments dealing with flow across fiber tows, only a thin strip along the fiber tow circumference was filled (practically instantaneously), when the primary front has passed over the tow [2,3,6]. We can confirm such situation numerically and suggest resin and process parameters ensuring much favorable tow infiltration.

Two different inlet situations were chosen and applied to a specimen 6 mm long with three fiber tows of elliptical cross-section having semi-axes equal to 0.8 and 0.35 mm: constant inflow velocity of 20 and 1 mm/s. Intra-tow porosity, viscosity, surface tension and contact angle were kept the same as 0.4, 50 mPa s, 20 mN/m and 60°, respectively, giving N_{ci} equal to 0.05 and 0.003. Intra-tow permeability was chosen as 1.6×10^{-7} mm^2, which implies that single fibers have diameter of 14.7 μm and intra-tow capillary pressure corresponds to 1.9 kPa.

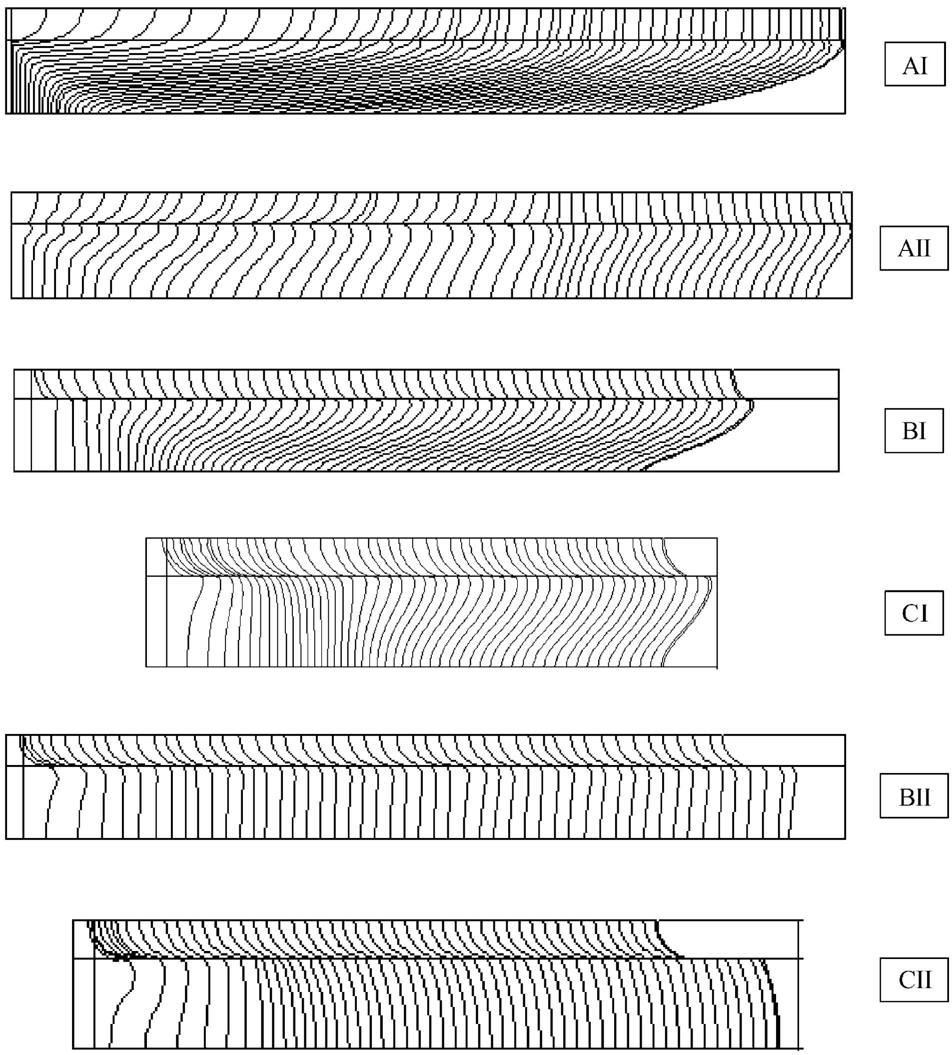

Fig. 11. Flow front pattern for cases AI, AII, BI, CI, BII and CII, respectively.

Flow front pattern and final filling stage are shown in Figs. 14 and 15. It is clearly seen that for lower inter-tow capillary number, tow filling is only slightly delayed with respect to the primary front, while for high N_{ci} tow infiltration practically stops.

4.5. Comparisons

It can be seen that in flows along fiber tows with constant inlet pressure, as resin advances, hydrodynamic pressure gradient in Stoke's region decreases, while capillary action remains the same. Therefore after some initial period, Δz starts to decrease. Separation of homogenized (stabilized) and transition region is thus better seen in cases with constant inflow velocity. In such cases, there is always present an initial, homogenized and transition region. Initial and transition regions behave in similar ways. Both adapt by radial flow either inlet or free front conditions. Once they are formed, they keep their depth, this is clearly seen in Fig. 13, where in cases B and C wick front delay or advance stabilized and keeps its value in later parts of the graph. Homogenized (stabilized) region extends along infiltration and no radial flows are present there.

Similar situation can be observed in flows across fiber tows, although transition region changes its characteristics periodically.

It should also be remarked that the ideal numerical simulations presented in this article do not justify voids formation, which need some additional perpendicular impulse in form of stitching or other fiber tows in woven fabric [4,5] or defects [3].

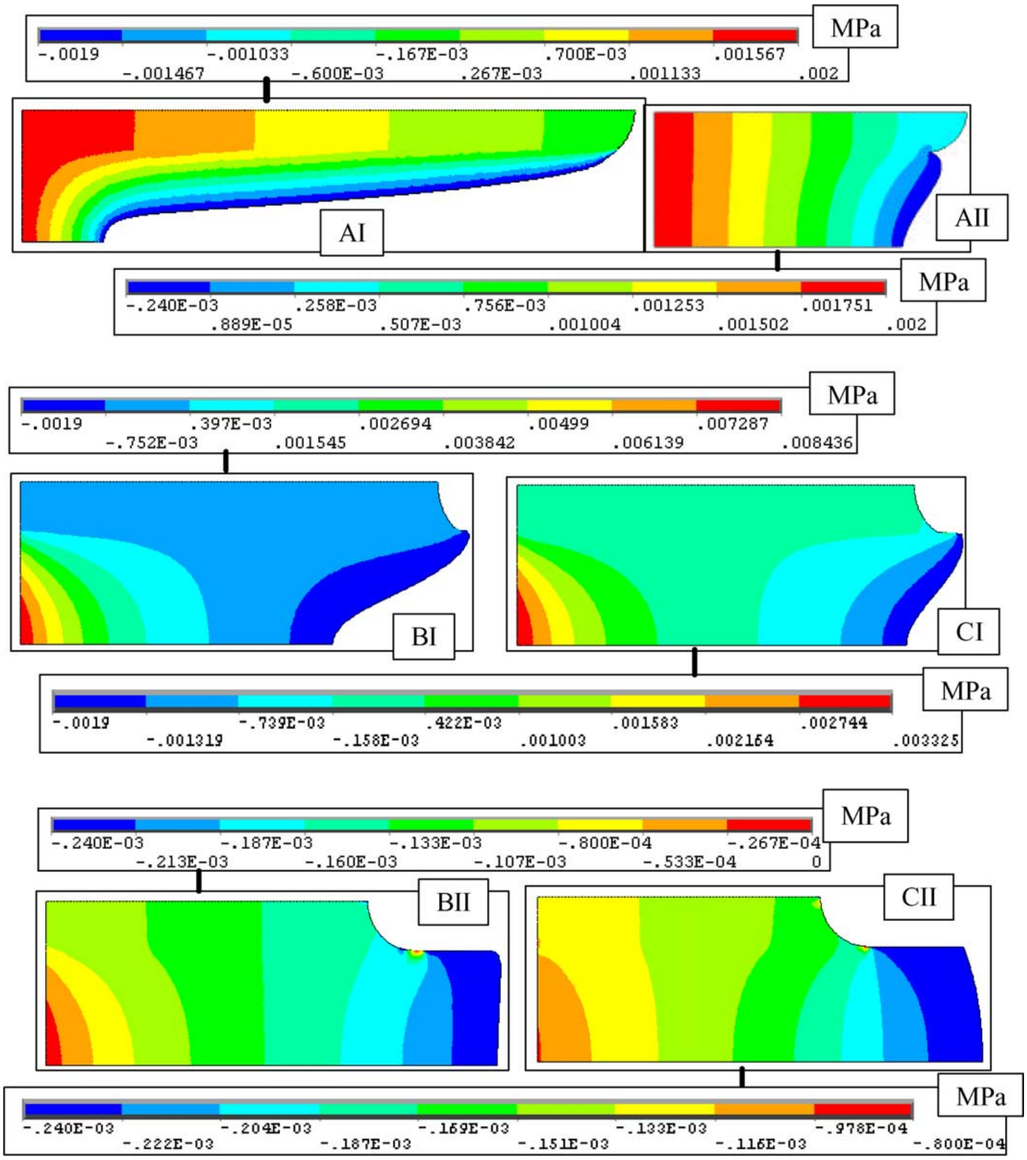

Fig. 12. Pressure distribution for selected intermediate stage for cases AI, AII, BI, CI, BII and CII, respectively (thick short lines link the contour legend to the corresponding figure).

5. Conclusions

In this article an analysis of the transition region formation and evolution during the resin impregnation stage of LCM process was presented. Numerical results at the mesolevel were obtained by FBP, which can track the advance of the resin front accurately by accounting for the surface tension effects at the boundary. FBP integrates routines and interconnecting moduli written in Ansys Parametric Design Language (APDL), FORTRAN and Maple and applies directly to FLOTRAN CFD ANSYS module to resolve a base analysis. Currently only two-dimensional problems or problems with rotational symmetry can be treated; extension to three dimensions is a subject for further research. No problems were detected at the interface $\Gamma_{t_k}^{S-B}$.

It should be stressed that FBP belongs to the group of moving mesh algorithms with remeshing of the filled domain at each time step, because free front curvature has been found essential to introduce correct surface tension effects. FBP has possibility of restarting the analysis from a specified time step and of modifying parameters related to the analysis for each time step. Implemented stabilization techniques are directed by

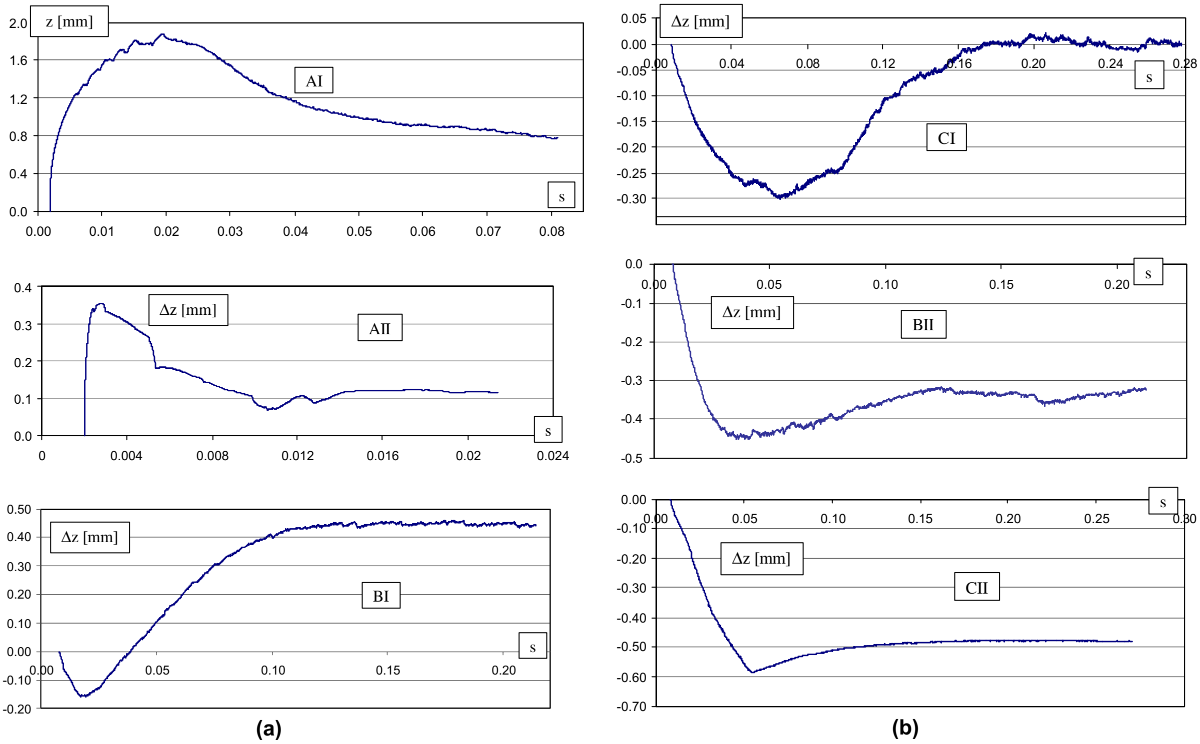

Fig. 13. Wicking front delay or advance Δz (positive for filling delay) with respect to filling time for cases AI, AII, BI, CI, BII and CII, respectively.

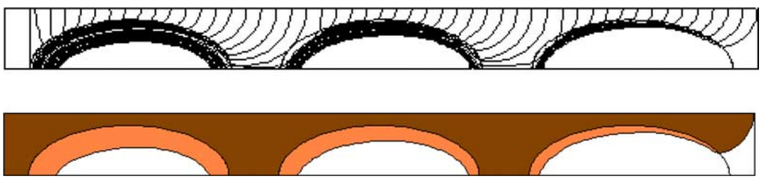

Fig. 14. Flow front pattern and final filling stage (different color designates resin in inter- and intra-tow spaces) in flow across fiber tows with $N_{ci} = 0.05$.

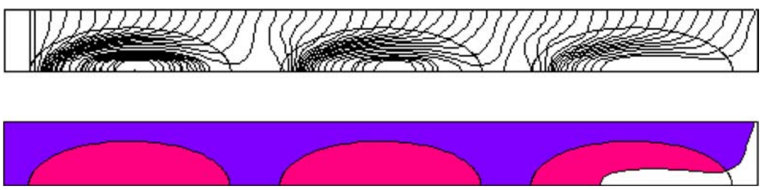

Fig. 15. Flow front pattern and final filling stage (different color designates resin in inter- and intra-tow spaces) in flow across fiber tows with $N_{ci} = 0.003$.

used specified values. FBP has full capability of capturing voids formation and of prediction process and material parameters for favorable filling without danger of dry spots formation. In posterior applications shear thinning fluids, coupling with thermal analysis and inclusion of fiber deformation will be examined.

Numerical simulations presented in this article clearly showed that wicking flows play an important role in fiber tows infiltration and cannot be omitted at the mesolevel scale. In flows along fiber tows it was demonstrated and concluded that tows impregnation is not ensured only by radial flows. Longitudinal wicking flows inside intra-tow spaces are important and must be considered. Cases with equilibrated flow front or advanced wick front, which are confirmed experimentally, and which are shown here in numerical simulations, would not be possible to justify without longitudinal wicking flows inside intra-tow spaces. Numerical results presented in this article were found in good agreement with the experimental studies presented elsewhere.

Additional studies must be dedicated to the correctness of the numerical treatment of the tow surface in cases when inter- and intra-tow flow fronts are completely separated. Also a possible formation of a contact angle on the tow surface should be considered. Either known phenomena from experimental observations can be modeled, or tow "surface" will have to be studied at microscale or even at nanoscale by molecular dynamics.

There is no basis for flow interference with neighboring tows, either in flows along or across the tows; therefore generalizations can be drawn from the simple examples presented in this article. Unfortunately, constant pressure or constant flow rate inlet conditions can hardly reproduce the real situation in the neighborhood of the macroscopic flow front.

Acknowledgements

Firstly named author would like to thank to the Portuguese institution for founding research Fundação para a Ciência e a Tecnologia for the scholarship allowing developing this work.

References

[1] Advani SG, Bruschke MV, Parnas RS. Resin transfer molding. In: Advani SG, editor. Flow and rheology in polymeric composites manufacturing. Amsterdam: Elsevier Publishers; 1994. p. 465–516.
[2] Parnas RS, Phelan FR. The effect of heterogeneous porous media on mold filling in resin transfer molding. SAMPE Quart 1991;22:53–60.
[3] Parnas RS, Salem AJ, Sadiq TAK, Wang HP, Advani SG. The interaction between micro- and macroscopic flow in RTM preforms. Compos Struct 1994;27:93–107.
[4] Patel N, Lee LJ. Effects of fiber mat architecture on void formation and removal in liquid composite molding. Polym Compos 1995;16:386–99.
[5] Patel N, Rohatgi V, Lee LJ. Micro scale flow behavior and void formation mechanism during impregnation through a unidirectional stitched fiberglass mat. Polym Eng Sci 1995;35:837–51.
[6] Sadiq TAK, Advani SG, Parnas RS. Experimental investigation of transverse flow through aligned cylinders. Int J Multiphase Flow 1995;21:755–74.
[7] Binetruy C, Hilaire B, Pabiot J. The interactions between flows occurring inside and outside fabric tows during RTM. Compos Sci Technol 1997;57:587–96.
[8] Binetruy C, Hilaire B, Pabiot J. The influence of fiber wetting in resin transfer molding: scale effects. Polym Compos 2000;24:548–57.
[9] Chan AW, Morgan RJ. Modeling preform impregnation and void formation in resin transfer molding of unidirectional composites. SAMPE Quart 1992;23:48–52.
[10] Chan AW, Morgan RJ. Tow impregnation during resin transfer molding of bi-directional nonwoven fabrics. Polym Compos 1993;14:335–40.
[11] Advani SG, Dimitrovová Z. Role of capillary driven flow in composite manufacturing. In: Hartland S, editor. Surface and interfacial tension; measurement, theory and application. Marcel Dekker, Surfactant Science Series Volume 119, pp. 263–312, 2004.
[12] Dimitrovová Z, Advani SG. Analysis and characterization of relative permeability and capillary pressure for free surface flow of a viscous fluid across an array of aligned cylindrical fibers. J Colloid Interf Sci 2002;245:325–37.
[13] Spaid MAA, Phelan FR. Modeling void formation dynamics in fibrous porous media with the Lattice Boltzman method. Composites A 1998;29A:749–55.
[14] Sanchez-Palencia E. Non-homogeneous media and vibration theory. Lecture Notes in Phys 1980;127:129–57.
[15] Ene HI, Polisevski D. Thermal flow in porous media. Dordrecht: D. Reidel Publishing Company; 1987.
[16] Calado VMA, Advani SG. Effective permeability of multilayer preforms in resin transfer molding. Compos Sci Technol 1996;56:519–31.
[17] Bruschke MV, Advani SG. A finite element/control volume approach to mold filling in anisotropic porous media. Polym Compos 1990;11:291–304.
[18] Bruschke MV, Advani SG. A numerical approach to model non-isothermal, viscous flow with free surfaces through fibrous media. Int J Numer Methods Fluids 1994;19:575–603.
[19] Hirt CW, Nichols BD. Volume of fluid (VOF) method for the dynamics of free boundaries. J Comput Phys 1981;39:201–25.
[20] White FM. Fluid mechanics. McGraw-Hill; 1994.
[21] Whitham GB. Linear and nonlinear waves. New York: John Wiley; 1974. p. 431–84 [Chapter 13].
[22] Lin M, Hahn HT, Huh H. A finite element simulation of resin transfer molding based on partial nodal saturation and implicit time integration. Composites A 1998;29A:189–98.
[23] Shojaei A, Ghaffarian SR, Karimian SMH. Numerical simulation of three-dimensional mold filling process in resin transfer molding using quasi-steady state and partial saturation formulations. Compos Sci Technol 2002;62:861–79.
[24] Muskat M. The flow of homogeneous fluids through porous media. New York: McGraw-Hill; 1937.

[25] Collins RE. Flow of fluids through porous media. Reinhold Publishing Corporation; 1961.
[26] Han K. Analysis of dry spot formation and changes in liquid composite molding. Ph.D. theses, The Ohio State University, OH, USA, 1994.
[27] Chang W, Kikuchi N. Analysis of composite molding using the homogenization method. Comput Fluid Dynamics 1996;7:49–77.
[28] Simacek P, Advani SG. A numerical model to predict fiber tow saturation during liquid composite molding. Compos Sci Technol 2003;63:1725–36.
[29] Dimitrovová Z, Advani SG. Free boundary viscous flows at micro and mesolevel during liquid composites molding process. In: Proceedings of the 14th International Conference on Composites Materials, July 14–18, 2003, San Diego, CA, EUA. p. 598–9.
[30] Potter K. Resin transfer molding. London: Chapman & Hall; 1997.
[31] Dimitrovová Z, Faria L. Finite element modeling of the resin transfer molding process based on homogenization techniques. Comput Struct 2000;76:379–97.
[32] Ranganathan S, Phelan FR, Advani SG. A generalized model for the transverse fluid permeability in unidirectional fibrous media. Polym Compos 1996;17:222–30.
[33] Papathanasiou TD. A structure oriented micromechanical model for viscous flow through square arrays of fibre clusters. Compos Sci Technol 1996;56:1055–69.
[34] Scheidegger AE. The physics of flow through porous media. New York: The Macmillan Company; 1957.
[35] Kim J. Studies on liquid flow in fibrous assembles. Ph.D. thesis, The Princeton University, NJ, USA, 1987.
[36] Ahn KJ, Seferis JC, Berg JC. Simultaneous measurements of permeability and capillary pressure of thermosetting matrices in woven fabric reinforcements. Polym Compos 1991;12:146–52.